nature materials

ARTICLES

PUBLISHED ONLINE: 6 APRIL 2014 | DOI: 10.1038/NMAT3942

Observation of quadrupole helix chirality and its domain structure in $DyFe_3(BO_3)_4$

T. Usui[1], Y. Tanaka[2], H. Nakajima[1], M. Taguchi[2], A. Chainani[2], M. Oura[2], S. Shin[2], N. Katayama[3], H. Sawa[3], Y. Wakabayashi[1] and T. Kimura[1]*

Resonant X-ray diffraction (RXD) uses X-rays in the vicinity of a specific atomic absorption edge and is a powerful technique for studying symmetry breaking by motifs of various multipole moments, such as electric monopoles (charge), magnetic dipoles (spin) and electric quadrupoles (orbital). Using circularly polarized X-rays, this technique has been developed to verify symmetry breaking effects arising from chirality, the asymmetry of an object upon its mirroring. Chirality plays a crucial role in the emergence of functionalities such as optical rotatory power and multiferroicity. Here we apply spatially resolved RXD to reveal the helix chirality of Dy 4*f* electric quadrupole orientations and its domain structure in $DyFe_3(BO_3)_4$, which shows a reversible phase transition into an enantiomorphic space-group pair. The present study provides evidence for a helix chiral motif of quadrupole moments developed in crystallographic helix chirality.

It is well known that chirality often plays a critical role in various disciplines, such as biology, organic chemistry and particle physics[1,2]. In contrast, chirality in solid-state physics, which is largely concerned with crystals possessing periodic arrays of atoms, has attracted less attention. This is partly because most of the physical properties of crystals are only weakly sensitive to their chirality. In fact, Neumann's principle[3] states that the symmetry of any physical property of a crystal must include the symmetry element of the crystal's 'point group', in which the screw rotation operation related to the helix chirality is neglected. Indeed, in connection with this insensitivity, there are very few methods to detect and identify the handedness embedded in crystals (except for optical activity[4] and X-ray diffraction using dispersion corrections[5]). In recent years, however, resonant X-ray diffraction (RXD) with circularly polarized X-rays has developed as a valuable technique to identify the handedness in helix chiral structures through a coupling of X-ray helicity with an enantiomorphic screw axis[6,7]. The first experimental demonstration to distinguish the crystallographic helix chirality by RXD with circularly polarized X-rays was carried out for α-quartz (SiO_2) with an enantiomorphic space-group pair, $P3_121$ (right-handed screw; ref. 8) and $P3_221$ (left-handed screw), and subsequently in berlinite ($AlPO_4$) and elemental Te with the same space-group pair[9,10]. In crystals having the space-group pair $P3_121$ and $P3_221$, reflections $00l$ ($l \neq 3n$, n = integer) are forbidden in non-resonant X-ray diffraction, but allowed in RXD for certain X-ray energy ranges. By carefully examining the space-group forbidden reflections observed for the RXD with circularly polarized X-rays, one can identify the sign of the crystallographic helix chirality[6–10]. More recently, using a highly focused X-ray beam, this technique was applied to image chiral domain structures of $CsCuCl_3$ with a $P6_122$ and $P6_522$ enantiomorphic space-group pair[11].

Compared with measurements of the optical activity and X-ray diffraction using dispersion corrections, RXD measurement with circularly polarized X-rays has the advantage of being able to detect not only crystallographic helix handedness but also the chirality ascribed to the periodic motif of multipole moments, such as magnetic dipoles and electric quadrupoles[12–14]. In the case of magnetic dipoles, the handedness of a 'helical magnetic structure' represents an example of chirality in magnetic crystals which can be identified by the RXD technique using circularly polarized X-rays[15–17]. Furthermore, recent extensive studies on magnetic crystals revealed that the chirality (or the handedness) of complex magnetic orderings, such as helical magnetic order, has a unique impact on the dielectric and transport properties, leading to unusual phenomena such as multiferroicity[18,19] and anomalous magnetotransport[20]. Thus, during these years, the concept of chirality has moved to the forefront of solid-state physics.

In this study, we show the chiral motif of quadrupole moments and its domain structure by means of the RXD technique using a circularly polarized, micro-focused X-ray beam. For this purpose, we employed single-crystal specimens of $DyFe_3(BO_3)_4$ having dysprosium 4*f* quadrupole moments and enantiomorphs with right-handed and left-handed helical structures[21]. This ferroborate crystallizes in a trigonal space group, $R32$, in which a Dy^{3+} ion is surrounded by a trigonal prism of six O^{2-} ions. On cooling, it undergoes a first-order structural phase transition into an enantiomorphic space-group pair ($P3_121$ and $P3_221$), which is the same as that in α-quartz, at $T_s \approx 285$ K (refs 22,23). In the $P3_121$ or $P3_221$ structure of $DyFe_3(BO_3)_4$, not only Fe^{3+} ions but also Dy^{3+} ions are arranged in a right-handed or left-handed helical manner along the three-fold c axis[22]. For our samples, we have clearly observed the structural transition at T_s as a sharp peak anomaly in specific heat and the appearance of the Bragg reflection $\bar{2}04$, as shown in Fig. 1a. On further decreasing the temperature (T), the specific heat shows another anomaly at the Néel temperature $T_N = 38$ K, where an antiferromagnetic (AF) order for both Fe and Dy moments develops[22]. In the AF phase, $DyFe_3(BO_3)_4$ exhibits a magnetoelectric effect accompanied by a spin flop[24]. In this work, we show that chirality due to the orientation of the quadrupole moment

[1]Division of Materials Physics, Graduate School of Engineering Science, Osaka University, Toyonaka, Osaka 560-8531, Japan, [2]RIKEN SPring-8 Center, Sayo, Hyogo 679-5148, Japan, [3]Department of Applied Physics, Graduate School of Engineering, Nagoya University, Nagoya 464-8603, Japan.
*e-mail: kimura@mp.es.osaka-u.ac.jp

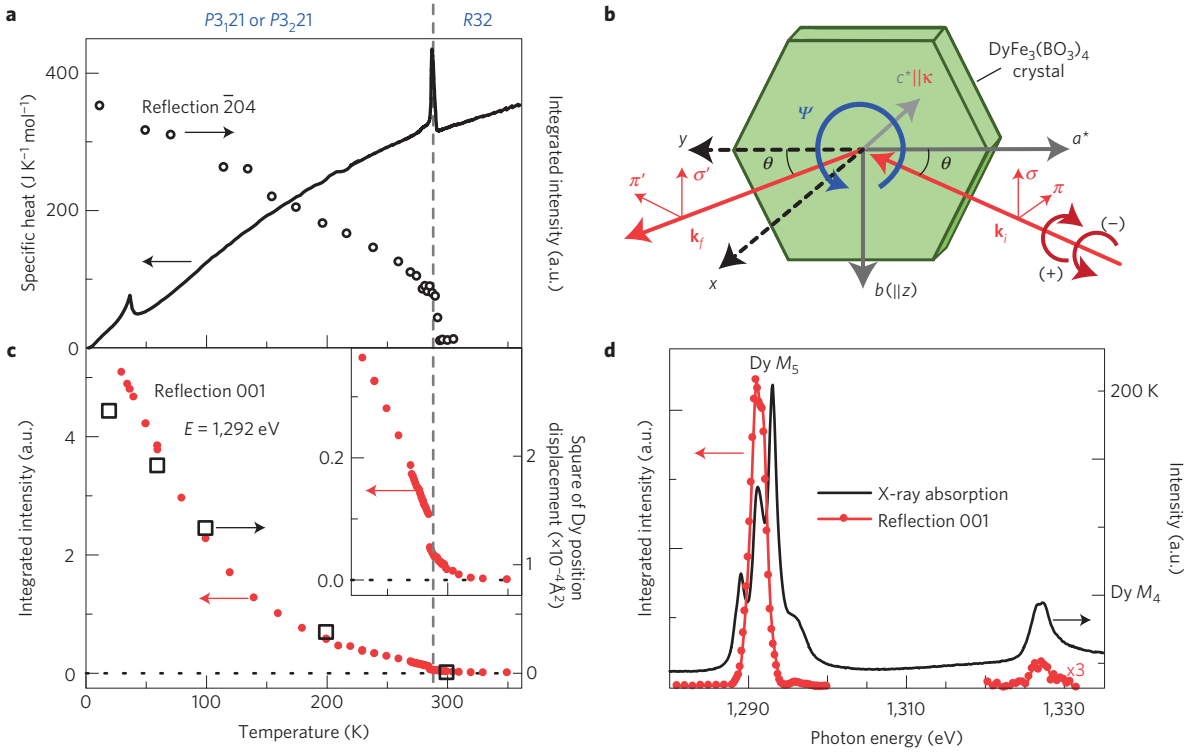

Figure 1 | Characterization of the structural phase transition using specific heat, non-resonant diffraction, and resonant diffraction at the Dy $M_{4,5}$ absorption edges. a, Specific heat and integrated intensity of reflection $\bar{2}04$ as a function of T. Reflection $\bar{2}04$ was taken using non-resonant X-ray diffraction with Mo $K\alpha$ X-rays. **b**, Schematic illustration of the scattering geometry for the present RXD measurements. Here $\mathbf{k}_i$ and $\mathbf{k}_f$ are the propagation vectors of the incident and diffracted X-rays, respectively. The azimuthal and Bragg angles are denoted by Ψ and θ, respectively. The origin of $\Psi = 0$ is defined by the a^* axis when it is parallel to $-(\mathbf{k}_i + \mathbf{k}_f)$. The σ (σ') and π (π') components are perpendicular and parallel to the scattering plane, respectively. **c**, T dependence of the integrated intensity of forbidden reflection 001 obtained by the RXD measurements with an incident X-ray energy of 1,292 eV. Open squares show the square of the displacement of the Dy position along the ξ axis from its position at 300 K (Supplementary Information). The inset shows a magnified region around T_s. **d**, The black line and red dots represent the spectra of the X-ray absorption and forbidden reflection 001, respectively, as a function of photon energy at 200 K.

sets in at $T_s \approx 285$ K and co-exists with the antiferromagnetic order below $T_N = 38$ K.

We prepared two crystals of $DyFe_3(BO_3)_4$ (Sample 1 and Sample 2) for the RXD measurements (Methods). The experimental set-up for the RXD measurements is illustrated in Fig. 1b, and is explained in detail in the Methods. Figure 1d shows the resonance enhancement of the forbidden reflection 001 at the Dy $M_{4,5}$ absorption edges and $T = 200$ K ($< T_s$) for Sample 1. To show the resonant edges, we overlay the corresponding X-ray absorption spectrum (XAS), in which three strong peaks and one weak peak appear around the Dy M_5 and M_4 edges, respectively. The three distinct features at the M_5 edge in XAS are ascribed to the dipole selection rules: $\Delta J = 0$ and ± 1 transitions[25] (Supplementary Information). Evidently, reflection 001 is strongly enhanced at the M_5 edge, whereas its enhancement at the M_4 edge is much smaller. (A similar energy profile has been reported for the $M_{4,5}$ edges of DyB_2C_2 at the antiferro-quadrupolar ordering reflection $00\frac{1}{2}$; ref. 26.) In the following experiments, therefore, the incident photon energy was tuned to the Dy M_5 edge ($E = 1,292$ eV), at which reflection 001 shows the maximum intensity. Figure 1c shows the T profile of reflection 001 measured at $E = 1,292$ eV (closed circles), which clearly demonstrates that the integrated intensity develops below T_s (see the inset of Fig. 1c) and that it increases drastically with decreasing T.

Figure 2b,c shows the 2θ–θ scan profiles of reflection 001 measured at two different sample positions on Sample 1. Closed and open symbols denote the data taken with (+) and (−) helical incident beams, respectively. The circular polarization state for helicity (+) ((−)) is expressed by a sum of the σ and π linear polarizations, in which the σ component is advanced (behind) in time by a quarter period with respect to the π component, as illustrated in Fig. 1b. A photograph of Sample 1 is shown in Fig. 2a. The two different positions are in the regions marked as α and β. These RXD measurements were carried out at $T = 200$ K ($< T_s$) and an azimuthal angle $\varphi = 0°$. Here, φ is the angle rotated with respect to the scattering vector $\boldsymbol{\kappa}$ ($\| c^*$), and its origin ($\varphi = 0°$) is defined as the configuration in which the scattering plane is parallel to the horizontal direction of the photo in Fig. 2a. As clearly seen in Fig. 2b,c, the sign change in the helicity of the circular polarization yields substantially different intensities of the forbidden reflection 001 for both the sample positions. Moreover, the helicity-dependent magnitude relations of the intensities are reversed for the two different sample positions. The intensity observed for incident X-rays with the positive (+) helicity is stronger than that with the negative (−) helicity in Fig. 2b, whereas the intensity for (+) helicity X-rays is weaker than that for the (−) helicity X-rays in Fig. 2c.

To further verify the sample position dependence of the chirality in Sample 1, we performed a microdiffraction scan along the y and z directions (Fig. 1b) with circularly polarized micro-focused beams, keeping the Bragg angle θ for reflection 001. Figure 2d–f shows two-dimensional yz-scanned intensity maps of the forbidden reflection 001 over a 1.5×1.5 mm^2 area at $\varphi = 0°$, 30° and 60°, respectively. The measurements have been done at 200 K. Red and blue colours correspond to high and low intensity, respectively. The intensity maps shown in the upper and lower panels in Fig. 2d–f were taken at almost the same sample area using (+) and (−) helical

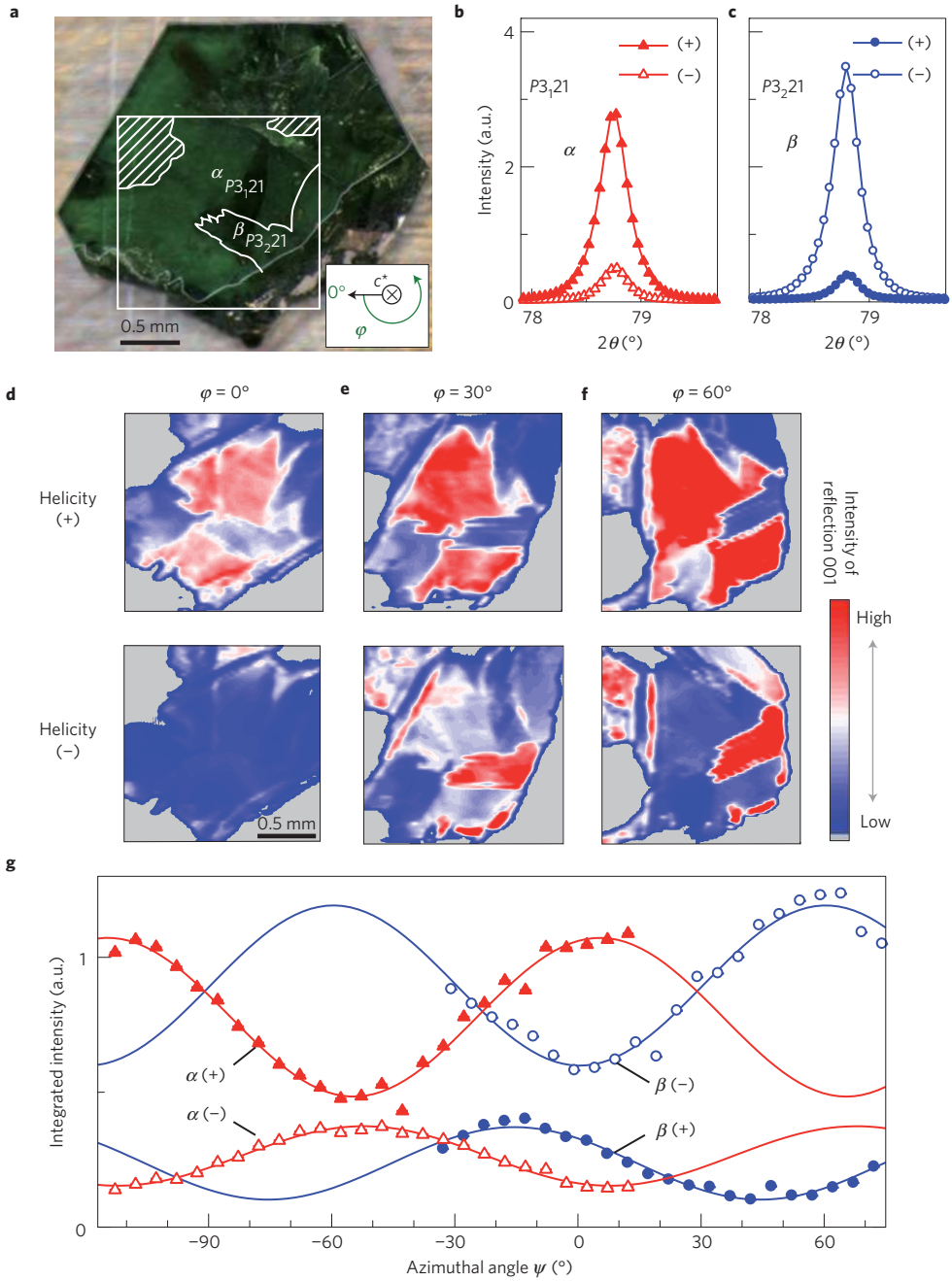

Figure 2 | Sample position and circular X-ray polarization dependence of the intensity of forbidden reflection 001 and spatial images of the crystallographic chiral domain structure at 200 K. a, Photograph of the scanned surface of Sample 1. At $\varphi = 0°$, the scattering plane is parallel to the a^* axis and the horizontal direction of the photo. **b**,**c**, The 2θ–θ scan profiles around reflection 001 from two different sample positions on Sample 1. These measurements were carried out at 200 K and $\varphi = 0°$ using (+) and (−) helical incident X-rays with an energy of 1,292 eV. **d**–**f**, X-ray intensity maps of the forbidden reflection 001 using (+) and (−) helical incident X-rays in the upper and lower panels, respectively. The data shown in **d**–**f** were obtained at $\varphi = 0°$, 30° and 60°, respectively. In **a**, the box denotes the scanned area for the data shown in **d**. Hatched areas represent the regions where the reflected X-ray intensity is weak because of the surface quality. **g**, Azimuthal angle dependence of the integrated intensity of reflection 001 measured in the regions α (red symbols) and β (blue symbols). Closed and open symbols denote the data obtained by using (+) and (−) helical incident X-rays, respectively. Solid lines represent the fit obtained with the model presented in the text.

incident X-rays, respectively. When comparing the intensity maps obtained by the (+) helicity X-rays (upper panels of Fig. 2d–f), the contrast of the images becomes gradually more intense on rotating φ from 0° to 60°. However, the patterns of all the images are qualitatively similar to one another. Furthermore, the colour contrast is reversed when the sign of the X-ray helicity is reversed (compare the upper and lower panels of Fig. 2e,f). By applying a theoretical analysis of RXD from crystals with right-handed $P3_121$ and left-handed $P3_221$ structures[8–10,13] to the observed results, we can identify the absolute crystallographic chirality of each region, as discussed below. The analysis reveals that regions α and β correspond to right-handed ($P3_121$) and left-handed ($P3_221$) chiral domains, respectively, and that Sample 1 is composed of multi-chiral domains. The size of the observed domains is on a (sub)millimetre scale. (The domain pattern is robust and does not change each time T_s is passed. This is because the crystallographic structure

is already chiral ($R32$) above T_s. Namely, both left- and right-handed crystals already exist in which FeO_6 octahedra form helix chains even above T_s, which governs the handedness below T_s and the robustness of chiral domains observed here.) Thus, we have successfully observed the helix chiral domains by scanning resonant X-ray microdiffraction with a focused, circularly polarized X-ray beam.

Next, we show the azimuthal angle dependence of the intensity of reflection 001, which is related to the above-mentioned change in the contrast of the intensity maps by varying φ. Figure 2g shows the integrated intensity of reflection 001 from regions α (red symbols) and β (blue symbols) in Sample 1 as a function of the azimuthal angle Ψ. These measurements have been done at 200 K using incident beams with both (+) and (−) helicities. In the graph, the origin of the horizontal axis ($\Psi = 0°$) is defined as the diffraction geometry where the b axis of each chiral domain is aligned along the z axis. Namely, the geometry at $\Psi = 0°$ is equivalent to that illustrated in Fig. 1b for the respective chiral domains. (The experimental set-up of the region β was consistent with that shown in Fig. 1b (namely, $\Psi = \varphi$), whereas that in region α corresponded to the configuration at $\Psi = \varphi - 60°$. Thus, in Fig. 2g the data for region α were shifted by −60°.) In all the data, a sinusoidal modulation exhibiting three-fold periodicity of the enantiomorphic screw-axis is observed. The integrated intensity and amplitude of the sinusoidal modulation by the (+) helicity X-rays are larger than those from the (−) helicity X-rays in the diffraction from region α (red triangles), whereas these relationships are reversed in the diffraction from region β (blue circles). Moreover, the phases of the sinusoidal modulation observed by the (+) and (−) X-ray helicities in region α show an anti-phase relation and are shifted by approximately +5 to +8° from the origin. In region β, the phase by the (+) X-ray helicity is shifted by approximately −15° from the origin whereas the shift observed by (−) X-ray helicity is negligible. The origin of these phase shifts will be discussed later.

Theoretical descriptions of the structural factor for the enantiomorphic space-group pair $P3_121$ and $P3_221$ have been discussed in detail[12,13]. According to the theory presented there, the intensity I as a function of Ψ for reflection 001 within the $E1E1$ resonant event is given by

$$I = I_0 + I_1 \cos(3\Psi) \tag{1}$$

$$I_0 = \frac{1}{2}\left\{A^2\left(1+\sin^2\theta\right)^2 + 2B^2\right\} + \frac{1}{2}P_3A^2\left(1+\sin^2\theta\right)\cos^2\theta + P_2\nu A^2\sin\theta\left(1+\sin^2\theta\right) \tag{2}$$

$$I_1 = AB(2P_3\sin\theta - P_2\nu\cos^2\theta) \tag{3}$$

Here the Bragg angle θ and the Stokes parameters P_2 and P_3, the circular and the linear polarization, respectively, are given by the experimental configuration. These values are described in Methods. The parameter ν denotes the crystallographic chirality ($\nu = +1$ for $P3_121$ and $\nu = -1$ for $P3_221$). The $P_2\nu$ term plays a crucial role in identifying the absolute chirality. The parameters A and B are given by the two independent Dy quadrupole components as $A = 3/2Q_{\xi^2-\eta^2}$ and $B = 3/2Q_{\eta\zeta}\cos\theta$. The quadrupole consists of five independent components, $Q_{\xi^2-\eta^2}$, $Q_{\xi\eta}$, $Q_{\eta\zeta}$, $Q_{\zeta\xi}$, and $Q_{3\zeta^2-r^2}$ with respect to the right-handed orthonormal quantization axes ($\xi\eta\zeta$) defined on the reference site $(-x,-x,0)$ for both the space groups. Here the ξ axis coincides with the two-fold axis [110] and the ζ axis coincides with the c axis. This definition is the same as that in ref. 13. The crystal axes (abc) in the trigonal system are defined using the atomic coordinates (Supplementary Information) to avoid the 60° arbitrariness in the choice of the unit cell. We find that the two-fold symmetry along the ξ axis (C_2 site symmetry) makes $Q_{\xi\eta} = Q_{\zeta\xi} = 0$. According to the selection rule[13], the component $Q_{3\zeta^2-r^2}$ contributes to reflections $00l$ ($l = 3n$) and the components $Q_{\xi^2-\eta^2}$ and $Q_{\eta\zeta}$ contribute to forbidden reflections $00l$ ($l = 3n \pm 1$). The components $Q_{\xi^2-\eta^2}$ and $Q_{\eta\zeta}$ at the two other Dy sites located at $(x,0,\pm1/3)$ and $(0,x,\mp1/3)$ are obtained by rotations of +120° and −120° about the c axis, respectively. The upper (lower) sign of 1/3 corresponds to the space group $P3_121$ ($P3_221$). (See the top and middle panels of Fig. 3.)

Thus the chirality parameter ν as well as the values of the quadrupole components, $Q_{\xi^2-\eta^2}$ and $Q_{\eta\zeta}$, in arbitrary units are determined by fitting the experimental results shown in Fig. 2g to equations (1)–(3). However, the experimental data deviate slightly from the curves expected by equation (1), in terms of the phase shift mentioned above, which predicts that the reflection intensity has a maximum or a minimum at $\Psi = 0°$. Possible origins of such a phase shift in the Ψ dependence of RXD have been discussed in terms of several mechanisms such as the contribution of parity-odd resonant events, such as $E1E2$ for α-quartz and berlinite[9,13], and the birefringence for CuO (ref. 27). Ref. 7 suggests a combined effect of the core-hole lifetime and the symmetry of the wavefunction of the intermediate states for α-quartz. In the case of $DyFe_3(BO_3)_4$, resonant scattering at the Dy M_5 edge is mainly governed by the $E1E1$ event because the XAS spectrum at the Dy M_5 edge is explained well by the $E1$ transition (Supplementary Information). The contribution of the birefringence[27] may cause a phase shift in the Ψ dependence. However, further theoretical consideration is needed to clarify the origin of the phase shift observed in $DyFe_3(BO_3)_4$.

In the following analysis, we introduce a phase shift angle $\delta(P_2, \nu)$ as a fitting parameter,

$$I = I_0 + I_1\cos\{3[\Psi - \delta(P_2,\nu)]\} \tag{4}$$

First, by using equations (2)–(4), we analyse the Ψ dependence of the integrated intensity of reflections for Sample 1. Obviously, all the data shown in Fig. 2g can be nicely fitted with equation (4), which allows us to obtain I_0 and I_1. Then, the sign of the crystallographic chirality ν is determined by checking the difference between I_0 obtained by the (+) and the (−) helicity. Namely,

$$\Delta I_0 = I_0(+P_2) - I_0(-P_2) = 2P_2\nu A^2\sin\theta\left(1+\sin^2\theta\right) \tag{5}$$

As seen in Fig. 2g, the sign of ΔI_0 for the region α is positive whereas that for the region β is negative. From equation (5), this means that the chirality of the region α is $\nu = +1$ ($P3_121$) whereas that of β is $\nu = -1$ ($P3_221$). In Table 1, we list I_0 and I_1 obtained from the fits of the data shown in Fig. 2g to equation (4) (I_0^{exp} and I_1^{exp}) as well as those obtained from equations (2) and (3) (I_0^{cal} and I_1^{cal}) with the experimental parameters. One of the most interesting observations in Table 1 is that the signs of I_1^{exp} at α($\nu = +1$) are opposite to those at β($\nu = -1$). For example, $I_1^{exp}(+\nu, +P_2) = 0.294$ whereas $I_1^{exp}(-\nu, -P_2) = -0.297$. This sign inversion indicates that equation (3) satisfies the relation $I_1(+\nu, \pm P_2) = -I_1(-\nu, \mp P_2)$ or the product $Q_{\xi^2-\eta^2}Q_{\eta\zeta}$ has opposite signs for region α($\nu = +1$) and region β($\nu = -1$). This feature is due to an intrinsic property between the enantiomorphic space-group pair. The axes ($\xi\eta\zeta$) defined at the reference site are right-handed for both the space-groups whereas the DyO_6 clusters located at the reference site are not the same for the enantiomorphic space-groups. The DyO_6 cluster has a mirror image of each other in terms of the $\zeta\xi$ plane, as illustrated in the top panels in Fig. 3a,b. The mirror operation with respect to the $\zeta\xi$ plane gives $Q_{\xi^2-\eta^2}(\nu = +1) = Q_{\xi^2-\eta^2}(\nu = -1)$ and $Q_{\eta\zeta}(\nu = +1) = -Q_{\eta\zeta}(\nu = -1)$. The relations are in good accord with the experimental results $Q_{\xi^2-\eta^2} \cong -0.37$ and $Q_{\eta\zeta} \cong +0.42$ for region α, and $Q_{\xi^2-\eta^2} \cong -0.41$ and $Q_{\eta\zeta} \cong -0.39$ for region β. The values are given by the equations $I_i^{cal} = I_i^{exp}$ ($i = 0, 1$). Thus, these relations, together with other similar relations between

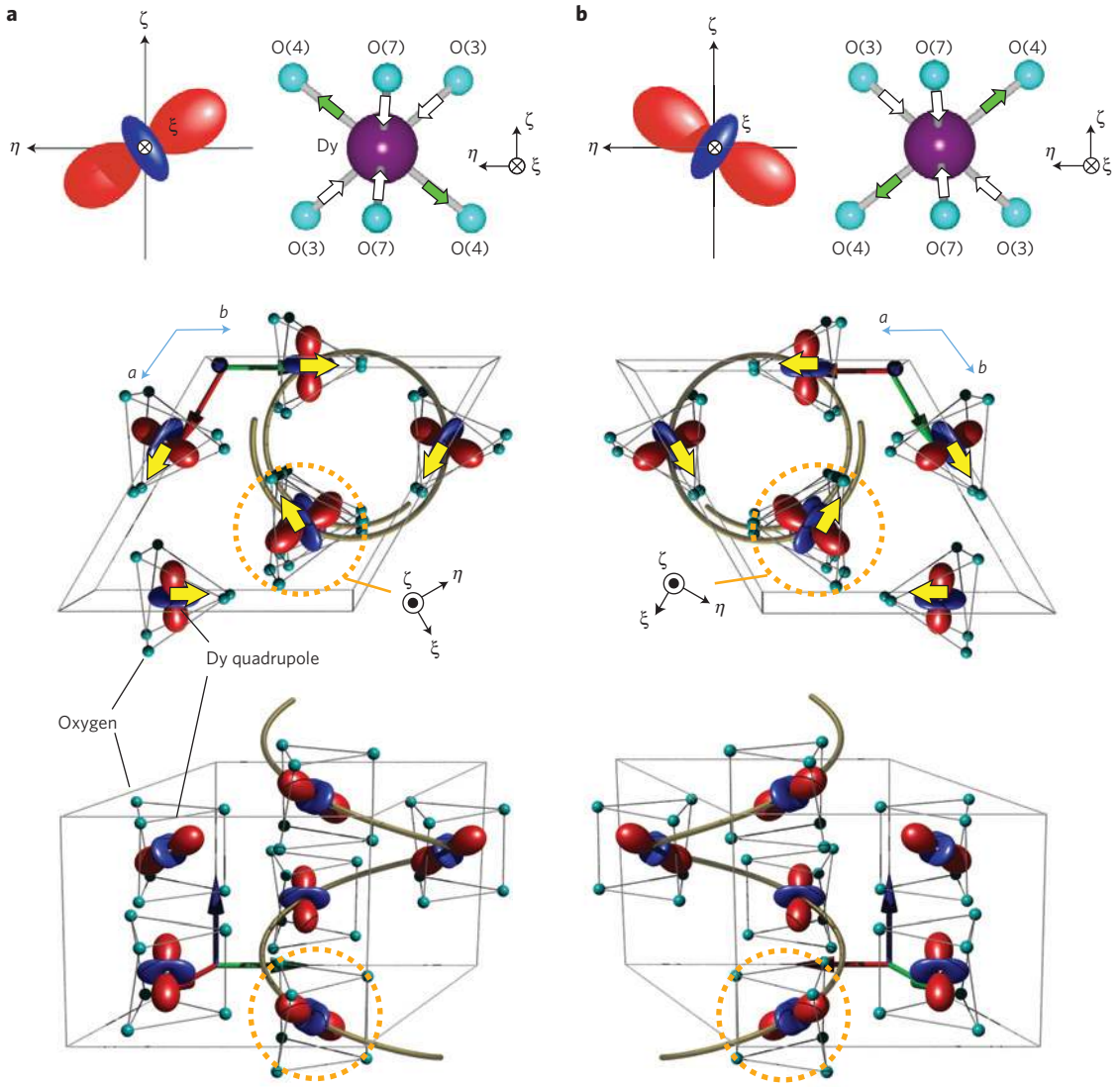

Figure 3 | Helix chiral motif of quadrupole moments. a,b, Schematic illustrations of left-handed ($P3_221$) (**a**) and right-handed ($P3_121$) (**b**) chiral structures and proposed quadrupole helix chirality in $DyFe_3(BO_3)_4$. Top panels show the possible electric quadrupole states of Dy 4*f* electrons (lobes) and the deformation towards lower *T* in DyO_6 prisms surrounded by orange dotted circles in the middle and lower panels. The quadrupole component $Q_{\eta\zeta} > 0$ for $P3_121$ and $Q_{\eta\zeta} < 0$ for $P3_221$, respectively, and the quadrupole component $Q_{\xi^2-\eta^2} < 0$ for both structures. In the illustration of electric quadrupole states (top), red and blue parts denote positive and negative charge distribution, respectively. Green arrows represent elongation of the Dy–O bonds and white arrows represent contraction of the Dy–O bonds. The middle panels depict views along the *c* axis and bottom panels show the side views. Only Dy and O atoms are shown. Yellow arrows denote the electric quadrupoles and the displacements of the respective Dy atoms accompanied by the structural phase transition below T_s. Grey helices are guides for the eyes to visualize the helical chirality. Some illustrations were drawn by using VESTA (ref. 35).

Table 1 | I_0 and I_1 obtained from the fits of the data shown in Fig. 2g to equation (4) (I_0^{exp} and I_1^{exp}) as well as the experimental coefficients in equations (2) and (3) (I_0^{cal} and I_1^{cal}) for Sample 1.

Region	ν	P_2	I_0^{exp}	I_0^{cal}	I_1^{exp}	I_1^{cal}
α	+1	−0.944	0.264	$0.074A^2+B^2$	−0.110	$0.353AB$
		+0.944	0.778	$1.76A^2+B^2$	0.294	$-0.770AB$
β	−1	−0.944	0.895	$1.76A^2+B^2$	−0.297	$-0.770AB$
		+0.944	0.236	$0.074A^2+B^2$	0.134	$0.353AB$

the electronic structures of the two enantiomorphs, give insight into similarities and differences between the enantiomorphs as discussed in ref. 13, and suitably describe the present results of quadrupole helix chirality.

Figure 4 shows the integrated intensity of reflection 001 as a function of Ψ at various temperatures. For these measurements, we used Sample 2, which has a monochiral domain (Supplementary Information). The Ψ dependence in Sample 2 is equivalent to that of region β in Sample 1 for both the X-ray helicity (+) and (−). Thus, the chirality of Sample 2 is the same as that of region β, and $\nu = -1$ ($P3_221$). With decreasing *T*, the integrated intensity and the amplitude of the sinusoidal modulation increase monotonically, but overall features such as the periodicity and the phase shift do not change. The temperature evolution leads to a steep increase of the integrated intensity of reflection 001 towards lower temperatures, as seen in Fig. 1c. To discuss the observed dependence on *T*, we analysed the data shown in Fig. 4. Table 2 lists the parameters obtained from the aforementioned fitting procedures using equations (2) and (3). Both the amplitudes of I_0 and I_1 gradually increase with decreasing *T*. Using these parameters, we

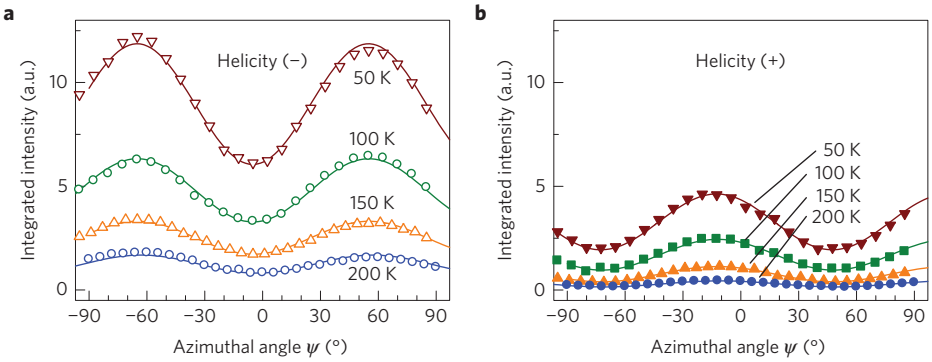

Figure 4 | Azimuthal angle dependence of the integrated intensity of forbidden reflection 001 at various temperatures for Sample 2 with nearly a monochiral domain ($P3_221$). a,b, The data shown were obtained by using (+) and (−) helical incident X-rays. Solid lines represent the fit obtained with the model presented in the text.

Table 2 | I_0 and I_1 obtained from the fits of the data shown in Fig. 4 to equation (4) (I_0^{exp} and I_1^{exp}) as well as the experimental coefficients in equations (2) and (3) (I_0^{cal} and I_1^{cal}) for Sample 2 composed of nearly a monochiral domain with the $P3_221$ space group ($\nu = -1$).

T (K)	P_2	I_0^{exp}	I_0^{cal}	I_1^{exp}	I_1^{cal}	$Q^2_{\xi^2-\eta^2}$	$Q^2_{\eta\zeta}$	$\frac{Q_{\eta\zeta}}{Q_{\xi^2-\eta^2}}$
200	−0.944	1.25	$1.76A^2+B^2$	−0.434	$-0.770AB$	0.25	0.19	0.9
	+0.944	0.297	$0.074A^2+B^2$	+0.146	$+0.353AB$			
150	−0.944	2.52	$1.76A^2+B^2$	−0.793	$-0.770AB$	0.46	0.51	1.1
	+0.944	0.765	$0.074A^2+B^2$	+0.367	$+0.353AB$			
100	−0.944	4.80	$1.76A^2+B^2$	−1.52	$-0.770AB$	0.82	1.16	1.20
	+0.944	1.70	$0.074A^2+B^2$	+0.741	$+0.353AB$			
50	−0.944	8.96	$1.76A^2+B^2$	−2.91	$-0.770AB$	1.49	2.27	1.23
	+0.944	3.29	$0.074A^2+B^2$	+1.31	$+0.353AB$			

have obtained the values of $Q^2_{\xi^2-\eta^2}$, ${Q_{\eta\zeta}}^2$ and $Q_{\eta\zeta}/Q_{\xi^2-\eta^2}$ at the respective temperatures. The absolute values of both quadrupole components $Q_{\xi^2-\eta^2}$ and $Q_{\eta\zeta}$ (both of which have negative values for $P3_221$) are enhanced with decreasing T, as shown in Fig. 4 and Table 2. Moreover, the increase of $Q_{\eta\zeta}/Q_{\xi^2-\eta^2}$ towards lower T suggests that the quadrupole component with the $\eta\zeta$ symmetry increases more rapidly than that with the $\xi^2-\eta^2$ symmetry.

In the left top panels of Fig. 3a,b, the charge distributions ascribed to the linear combination of $Q_{\xi^2-\eta^2}$ and $Q_{\eta\zeta}$ are schematically illustrated for the $P3_221$ and the $P3_121$ phases, respectively. The mirror relation of the charge distribution between these two phases is evident, which is attributed to the sign change in $Q_{\eta\zeta}$, as shown in the data of Fig. 2g and Table 1. The temperature evolution of $Q_{\xi^2-\eta^2}$ and $Q_{\eta\zeta}$ suggests that these types of charge distribution become more pronounced at Dy sites with decreasing T. This consideration is qualitatively supported by the T-dependent deformation of DyO_6 prisms. According to the results of our crystal structure analysis (Supplementary Information), the structural transition from the high-T $R32$ phase into the low-T $P3_121$(or $P3_221$) phase shifts the Dy site along the ξ axis, as denoted by thick yellow arrows in the middle panels of Fig. 3. Moreover, the structural transition causes elongation of the Dy–O(4) bonds and contraction of the Dy–O(3) and Dy–O(7) bonds. This deformation of the DyO_6 prism towards the low-T phase is indicated by thick arrows in the upper right panels of Fig. 3a,b. Comparing the left and right upper panels of Fig. 3a,b, it is likely that the deformation of the DyO_6 prism towards lower T is a result of stabilization of the quadrupoles with the $\xi^2-\eta^2$ and $\eta\zeta$ symmetries.

The deformation of the DyO_6 prism is, however, relatively smaller below 200 K than that observed at the phase transition at T_s (Supplementary Information), while the square of the Dy displacement from the special point of the $R32$ trigonal structure shows a similar temperature dependence to the intensity of reflection 001, proportional to the sum of the squares of the quadrupole components, as shown in Fig. 1c, suggesting a direct relation between the Dy displacement and its quadrupole components. On the other hand, the ${}^6H_{\frac{15}{2}}$ energy level of Dy^{3+} $4f$ electrons in $DyFe_3(BO_3)_4$ splits into eight Kramers doublets, and the splitting between the first and second sublevels is estimated to be $15 \sim 20\,cm^{-1}$ (refs 23,28–30). The temperature evolution of the intensity of reflection 001 may be affected by the population at the respective sublevels. More detailed experiments and discussions are needed for further quantitative understanding and will be the subject of future work.

In the middle and lower panels of Fig. 3, we illustrate the stabilized quadrupoles at the respective Dy sites in a unit cell of $DyFe_3(BO_3)_4$. These figures clearly show that not only Dy atoms but also the quadrupoles, including their orientations, are arranged in a helical manner. In addition, the handedness of the helical quadrupole arrangement in the $P3_221$ phase (Fig. 3a) is opposite to that in the $P3_121$ phase (Fig. 3b), which is derived by considering the correlation between the crystallographic chirality and the orientation of the charge distribution in each quadrupole. Thus, the present resonant X-ray diffraction study with circularly polarized X-rays provides a new concept, 'helix chiral arrangement (or ordering) of quadrupole moments' and reveals its domain structure. In $4f$ electron systems, it is known that the anisotropy of magnetism cannot be described without the spin–orbit interactions. Therefore, it is reasonable to consider that the direction of magnetic moments in the Dy sites of $DyFe_3(BO_3)_4$ is

strongly coupled with the orientation of its electric quadrupole, and that the observed helical quadrupole arrangement is linked to the 120°-type arrangement of Dy magnetic moments proposed by a previous neutron diffraction study[22]. In addition, the present study revealed the formation of fairly large domains (and/or a single domain) of quadrupole helix chirality in $DyFe_3(BO_3)_4$ single crystals. This can be related to the single magnetic chirality observed in a similar rare-earth ferroborate, $NdFe_3(BO_3)_4$, through the Dzyaloshinskii–Moriya interaction[31]. If we properly choose the compounds in which a phase transition from non-chiral to chiral structures takes place, control of the quadrupole helix chirality and its domain structures will be possible by external stimuli such as circularly polarized light, leading to unconventional material functionality.

Methods

Sample preparation and characterization. Single crystals of $DyFe_3(BO_3)_4$ were grown by a flux method using Bi_2O_3–MoO_3 flux, as reported previously[32]. The starting composition in wt.% was 20.0 Dy_2O_3, 12.7 Fe_2O_3, 18.7 B_2O_3, 25.2 Bi_2O_3 and 23.4 MoO_3. The mixture was put into a platinum crucible, heated at 1,000 °C in a furnace for 24 h, and melted completely. Next, a platinum rod was immersed into the melt and rotated for about 2 h to stir the flux. After the rod was withdrawn, some seed crystals were nucleated on the rod. After the nucleation was confirmed, the rod with seed crystals was immersed again into the melt heated at 1,000 °C. After holding at that temperature for 1 h, the melt was slowly cooled down to 968 °C, taking 13 days to grow crystals. Subsequently, the platinum rod with the grown crystals was pulled from the melt and cooled down to room temperature. The crystals were then leached from the flux with concentrated hydrochloric acid. All the above processes were carried out in air. The obtained crystals were greenish and had typical dimensions of approximately $2 \times 2 \times 2\,mm^3$.

We measured powder X-ray diffraction patterns of a crystal at room temperature and confirmed that its crystal structure belongs to the $R32$ trigonal structure. Some of the crystals were oriented with back-reflection Laue X-ray diffraction measurements and cut into thin plates with the widest faces perpendicular to the c axis (typical dimension about $2 \times 2 \times 0.5\,mm^3$). We mechanically polished their faces to a mirror-like surface for measurements of specific heat and resonant X-ray diffraction (RXD) with circularly polarized X-rays. The specific heat of one of the specimens was measured using a relaxation technique. Two of the specimens, termed Sample 1 and Sample 2, were chosen for the RXD measurements.

Resonant X-ray diffraction measurement with circularly polarized X-rays. For resonant X-ray diffraction (RXD) measurements with circularly polarized X-rays, we used two single-crystal specimens: Sample 1 and Sample 2. (The present study revealed that Sample 2 consists of a nearly monochiral domain with the $P3_221$ structure whereas Sample 1 is composed of multichiral domains with both $P3_121$ and $P3_221$ structures). Measurements on the polished surface of the two specimens were carried out using an ultrahigh-vacuum diffractometer equipped at the beamline 17SU, SPring-8, Japan[33]. The incident photon energy was tuned approximately to the Dy M_5 edge (=1,292 eV). The helicity of the incident beam was switched by the electromagnet of an undulator. In the present experimental setting, the Stokes parameters representing the polarization of the incident X-ray beam were $P_2 = +0.944$ and $P_3 = -0.164$ for (+) helicity X-rays and $P_2 = -0.944$ and $P_3 = -0.164$ for (−) helicity X-rays. (For ideal circularly polarized X-rays, $P_2 = +1(-1)$ and $P_3 \approx 0$ for positive (negative) helicity, whereas for linear σ (π) polarization $P_2 \approx 0$ and $P_3 = +1(-1)$.)

To observe forbidden reflection 001, these crystals were mounted with both the a^* and c^* axes in the scattering plane and the c^* axis along the scattering vector $\boldsymbol{\kappa}$ ($=\mathbf{k}_i - \mathbf{k}_f$, where $\mathbf{k}_i$ and $\mathbf{k}_f$ are the propagation vectors of the incident and diffracted X-rays), as illustrated in Fig. 1b. The azimuthal angle Ψ is a rotation of the sample about $\boldsymbol{\kappa}$. The Bragg angle θ for reflection 001 was observed at approximately 39° and was slightly dependent on T. The intensity of the diffracted X-rays was measured with a Si-photodiode sensor without polarization analysis. The penetration depth d_p of the incident beam into the crystal was estimated from the full-width at half-maximum ΔQ of reflection 001. Using the relation $d_p = 2\pi/\Delta Q$, where the unit of ΔQ is nm^{-1}, we obtained $d_p \sim 160$ nm.

For the chiral domain imaging, the crystals were positioned with an xyz translation stage with 25 μm step size, and the diffracted intensity of forbidden reflection 001 was measured at each point. (As depicted in Fig. 1b, the x direction is aligned antiparallel to the c^* axis and the z direction is perpendicular to the scattering plane.) We focused the incident X-ray beam using Kirkpatrick–Baez configuration mirrors equipped just before the diffractometer[34]. The beam size was approximately 30 μm in the horizontal direction and 15 μm in the vertical direction, giving spatial resolutions for the y and z scans of approximately 47 μm and 15 μm, respectively.

Crystal structure analysis. The single-crystal X-ray diffraction experiment was performed at BL02B1, SPring-8, Hyogo, Japan. The crystal used had a size of $140 \times 60 \times 20\,\mu m^3$. The wavelength of the incident X-rays was 0.5160 Å. A large imaging plate camera equipped with a He gas-flow type sample cooler was used. For image data processing and structure refinement, we used the programs RAPID AUTO and WinGX.

Received 19 November 2013; accepted 11 March 2014; published online 6 April 2014

References

1. Wagnière, G. H. *On Chirality and the Universal Asymmetry* (Wiley–VCH, 2007).
2. Barron, L. D. Chirality and life. *Space Sci. Rev.* **135,** 187–201 (2008).
3. Neumann, F. E. *Vorlesungen über die Theorie der Elastizität der festen Körper und des Lichtäthers* (B. G. Teubner-Verlag, 1885).
4. Condon, E. U. Theories of optical rotatory power. *Rev. Mod. Phys.* **9,** 432–457 (1937).
5. Bijvoet, J. M., Peerdeman, A. F. & van Bommel, A. J. Determination of the absolute configuration of optically active compounds by means of X-rays. *Nature* **168,** 271–272 (1951).
6. Lovesey, S. W. & Scagnoli, V. Chirality, magnetic charge and other strange entities in resonant X-ray Bragg diffraction. *J. Phys. Condens. Matter* **21,** 474214 (2009).
7. Igarashi, J. & Takahashi, M. Resonant X-ray scattering from chiral materials: alpha-quartz and alpha-berlinite. *Phys. Rev. B* **86,** 104116 (2012).
8. Tanaka, Y. *et al.* Right handed or left handed? Forbidden X-ray diffraction reveals chirality. *Phys. Rev. Lett.* **100,** 145502 (2008); *Phys. Rev. Lett.* **108,** 019901(E) (2012).
9. Tanaka, Y. *et al.* Determination of structural chirality of berlinite and quartz using resonant X-ray diffraction with circularly polarized X-rays. *Phys. Rev. B* **81,** 144104 (2010); *Phys. Rev. B* **84,** 219905(E) (2011).
10. Tanaka, Y. *et al.* Determination of the absolute chirality of tellurium using resonant diffraction with circularly polarized X-rays. *J. Phys. Condens. Matter* **22,** 122201 (2010).
11. Ohsumi, H. *et al.* Three-dimensional near-surface imaging of chirality domains with circularity polarized X-rays. *Angew. Chem.* **2013,** 125 (2013).
12. Lovesey, S. W., Balcar, E., Knight, K. S. & Fernández Rodríguez, J. Electronic properties of crystalline materials observed in X-ray diffraction. *Phys. Rep.* **411,** 233–289 (2005).
13. Lovesey, S. W., Balcar, E. & Tanaka, Y. Resonant diffraction of circularly polarized X-rays by a chiral crystal (low quartz). *J. Phys. Condens. Matter* **20,** 272201 (2008).
14. Lovesey, S. W. *et al.* Melting of chiral order in terbium manganite ($TbMnO_3$) observed with resonant X-ray Bragg diffraction. *J. Phys. Condens. Matter* **25,** 362202 (2013).
15. Gibbs, D., Moncton, D. E., D'Amico, K. L., Bohr, J. & Griier, B. H. Magnetic X-ray scattering studies of holmium using synchrotron radiation. *Phys. Rev. Lett.* **55,** 234–237 (1985).
16. Lang, J. C., Lee, D. R., Haskel, D. & Srajer, G. Imaging spiral magnetic domains in Ho metal using circularly polarized Bragg diffraction. *J. Appl. Phys.* **95,** 6537–6539 (2004).
17. Schierle, E. *et al.* Cycloidal order of 4*f* moments as a probe of chiral domains in $DyMnO_3$. *Phys. Rev. Lett.* **105,** 167207 (2010).
18. Cheong, S-W. & Mostovoy, M. Multiferroics: A magnetic twist for ferroelectricity. *Nature Mater.* **6,** 13–20 (2007).
19. Kimura, T. Spiral magnets as magnetoelectrics. *Annu. Rev. Mater. Res.* **37,** 387–413 (2007).
20. Nagaosa, N., Sirova, J., Onoda, S., MacDonald, A. H. & Ong, N. P. Anomalous Hall effect. *Rev. Mod. Phys.* **82,** 1539–1592 (2010).
21. Hinatsu, Y., Doi, Y., Ito, K., Wakeshima, M. & Alemi, A. Magnetic and calorimetric studies on rare-earth iron borates $LnFe_3(BO_3)_4$ (*Ln* = Y, La-Ns, Sm-Ho). *J. Solid State Chem.* **172,** 438–445 (2003).
22. Ritter, C., Pankrats, A., Gudim, I. & Vorotynov, A. A magnetic structure of iron borate $DyFe_3(BO_3)_4$: a neutron diffraction study. *J. Phys. Conf. Ser.* **340,** 012065 (2012).
23. Popova, E. A. *et al.* Magnetization and specific heat of $DyFe_3(BO_3)_4$ single crystal. *Euro. Phys. J. B* **62,** 123–128 (2008).
24. Popov, Yu. F. *et al.* Observation of spontaneous spin reorientation in $Nd_{1-x}Dy_xFe_3(BO_3)_4$ ferroborates with a competitive R-Fe exchange. *JETP Lett.* **89,** 345–351 (2009).

25. Goedkoop, J. B. *et al.* Calculations of magnetic X-ray dichroism in the 3*d* absorption spectra of rare-earth compounds. *Phys. Rev. B* **37,** 2086–2093 (1988).
26. Mulders, A. M. *et al.* High-order Dy multipole motifs observed in DyB_2C_2 with resonant soft X-ray Bragg diffraction. *J. Phys. Condens. Matter* **18,** 11195–11202 (2006).
27. Joly, Y., Collins, S. P., Grenier, S., Tolentino, H. C. N. & De Santis, M. Birefringence and polarization rotation in resonant X-ray diffraction. *Phys. Rev. B* **86,** 220101(R) (2012).
28. Stanislavchuk, T. N., Chukalina, E. P., Popova, M. N., Bezmaternykh, L. N. & Gudim, I. A. Investigation of the iron borates $DyFe_3(BO_3)_4$ and $HoFe_3(BO_3)_4$ by the method of Er^{3+} spectroscopic probe. *Phys. Lett. A* **368,** 408–411 (2007).
29. Volkov, D. V., Demidov, A. A. & Kolmakova, N. P. Magnetic properties of $DyFe_3(BO_3)_4$. *J. Exp. Theor. Phys.* **106,** 723–730 (2008).
30. Malakhovskii, A. V., Sukhachev, A. L., Strokova, A. Yu & Gudim, I. A. Magneto-optical activity of f–f transitions and properties of 4f states in single-crystal $DyFe_3(BO_3)_4$. *Phys. Rev. B* **88,** 075103 (2013).
31. Janoschek, M. *et al.* Single magnetic chirality in the magnetoelectric $NdFe_3(^{11}BO_3)_4$. *Phys. Rev. B* **81,** 094429 (2010).
32. Gudim, I. A., Eremin, E. V. & Temerov, V. L. Flux growth and spin reorientation in trigonal $Nd_{1-x}Dy_xFe_3(BO_3)_4$ single crystals. *J. Cryst. Growth* **312,** 2427–2430 (2010).
33. Takeuchi, T. *et al.* An ultrahigh-vacuum apparatus for resonant diffraction experiments using soft X-rays ($h\nu = 300$–$2,000$ eV). *Rev. Sci. Instrum.* **80,** 023905 (2009).
34. Ohashi, H. *et al.* Performance of a highly stabilized and high-resolution beamline BL17SU for advanced soft X-ray spectroscopy at SPring-8. *AIP Proc.* **879,** 523–526 (2007).
35. Momma, K. & Izumi, F. VESTA 3 for three-dimensional visualization of crystal, volumetric and morphology data. *J. Appl. Crystallogr.* **44,** 1272–1276 (2011).

Acknowledgements

The authors thank K. Haruki, T. Honda, Y. Shiratsuchi, M. Nagai, M. Ashida and H. Tada for their help in experiments, and K. Kimura for his enlightening discussions. This work was supported by KAKENHI (Grants No. 24244058, 25247054, and 23244074), MEXT, Japan. Resonant X-ray diffraction experiments were performed at beamline 17SU in SPring-8 with the approval of RIKEN (Proposal No. 3345 and 3394). Single-crystal X-ray diffraction experiments for crystal structure analysis were carried out at BL02B1, SPring-8 (Proposal No. 2013B0083).

Author contributions

T.U., Y.T. and T.K. initiated this work. T.U. and H.N. carried out sample preparation and characterization. N.K., H.S. and Y.W. performed crystal structure analysis. T.U. and Y.T. measured resonant X-ray diffraction and analysed the data with assistance from H.N., A.C., M.O. and S.S. M.T. calculated the X-ray absorption spectrum. Y.T. and T.K. designed and directed the research, and wrote the paper.

Additional information

Supplementary information is available in the online version of the paper. Reprints and permissions information is available online at www.nature.com/reprints. Correspondence and requests for materials should be addressed to T.K.

Competing financial interests

The authors declare no competing financial interests.